Received: 24 August 2022 | Revised: 12 January 2023 | Accepted: 13 January 2023

DOI: 10.1002/hipo.23512

RESEARCH ARTICLE

WILEY

Layer-specific mitochondrial diversity across hippocampal CA2 dendrites

Katy E. Pannoni[1] | Daniela Gil[1] | Mikel L. Cawley[1,2] | Mayd M. Alsalman[1] | Logan A. Campbell[1] | Shannon Farris[1,3,4]

[1]Fralin Biomedical Research Institute at Virginia Tech Carilion, Center for Neurobiology Research, Roanoke, Virginia, USA

[2]Graduate Program in Translational Biology, Medicine, and Health, Virginia Tech, Blacksburg, Virginia, USA

[3]Department of Biomedical Sciences and Pathobiology, Virginia-Maryland College of Veterinary Medicine, Virginia Tech, Blacksburg, Virginia, USA

[4]Virginia Tech Carilion School of Medicine, Roanoke, Virginia, USA

Correspondence
Shannon Farris, Fralin Biomedical Research Institute at Virginia Tech Carilion, Fralin Biomedical Research Institute at Virginia Tech Carilion, Center for Neurobiology Research, Roanoke, Virginia, USA.
Email: farrissl@vtc.vt.edu

Funding information
National Institute of Mental Health, Grant/Award Numbers: R00MH109626, R01MH124997; National Institutes of Health, Grant/Award Number: 1S10OD026838-01A1

Abstract

CA2 is an understudied subregion of the hippocampus that is critical for social memory. Previous studies identified multiple components of the mitochondrial calcium uniporter (MCU) complex as selectively enriched in CA2. The MCU complex regulates calcium entry into mitochondria, which in turn regulates mitochondrial transport and localization to active synapses. We found that MCU is strikingly enriched in CA2 distal apical dendrites, precisely where CA2 neurons receive entorhinal cortical input carrying social information. Furthermore, MCU-enriched mitochondria in CA2 distal dendrites are larger compared to mitochondria in CA2 proximal apical dendrites and neighboring CA1 apical dendrites, which was confirmed in CA2 with genetically labeled mitochondria and electron microscopy. MCU overexpression in neighboring CA1 led to a preferential localization of MCU in the proximal dendrites of CA1 compared to the distal dendrites, an effect not seen in CA2. Our findings demonstrate that mitochondria are molecularly and structurally diverse across hippocampal cell types and circuits, and suggest that MCU can be differentially localized within dendrites, possibly to meet local energy demands.

KEYWORDS
dendrites, entorhinal cortex, hippocampal CA2, mitochondrial calcium uniporter, mitochondrial localization, mitochondrial morphology

1 | INTRODUCTION

Mitochondria are critical organelles that are responsible for a variety of functions in the cell, including generating energy, regulating calcium homeostasis, and signaling apoptosis (Bock & Tait, 2020; Rizzuto et al., 2012; Spinelli & Haigis, 2018). There is mounting evidence of mitochondrial diversity across tissues and cell types and the functional significance of this heterogeneity is an area of active investigation (Fecher et al., 2019; Pekkurnaz & Wang, 2022; Sprenger & Langer, 2019). In neurons, mitochondria are important for synaptic transmission, maintenance, and plasticity (Devine & Kittler, 2018; Li et al., 2004; Stowers et al., 2002; Tang & Zucker, 1997). Mitochondria are commonly found in axon terminals, as well as other sites with high energetic demand, and the loss of presynaptic mitochondria results in defective synaptic transmission (Stowers et al., 2002). Less is known about the role of mitochondria at the post-synapse. Previous work demonstrated that the proper localization of mitochondria in cultured hippocampal neuron dendrites is also critical to support synapses. Specifically, increasing either mitochondrial content or mitochondrial activity in dendrites increased the number of spines and synapses (Li et al., 2004). In turn, synaptic activity can regulate the motility of mitochondria in

dendrites, leading to an accumulation of mitochondria near recently active synapses (Li et al., 2004). Interestingly, the morphology and the distribution of mitochondria differs between axons and dendrites in vivo and in vitro (Chang et al., 2006; Lewis et al., 2018), and mitochondria in the two compartments are differentially modulated by synaptic activity in culture (Chang et al., 2006). Although previous studies have looked at the morphological diversity of mitochondria in CA1, CA3 or Dentate Gyrus of the hippocampus (Faitg et al., 2021; Lee et al., 2022; Popov et al., 2005), this has not yet been studied in CA2.

We previously reported that CA2 of the hippocampus, a subregion that is essential for social memory (Dudek et al., 2016; Hitti & Siegelbaum, 2014; Stevenson & Caldwell, 2014), is enriched for transcripts related to mitochondrial function compared to neighboring subregions CA1, CA3, and Dentate gyrus, DG (Farris et al., 2019). In particular, we found that multiple components of the mitochondrial calcium uniporter (MCU) complex are enriched in CA2 (Farris et al., 2019). The MCU complex regulates calcium entry into the mitochondrial matrix (Baughman et al., 2011; Kamer & Mootha, 2015; Stefani et al., 2011), which can induce morphological (Han et al., 2008) and metabolic changes (Llorente-Folch et al., 2015; Wescott et al., 2019) and regulate the transport and localization of mitochondria to active synapses (Wang & Schwarz, 2009). Thus, enrichment of MCU in CA2 neurons may differentially influence mitochondrial morphology and localization to meet local energy demands.

In this study, we found that MCU expression was strikingly enriched in CA2 distal apical dendrites compared to proximal apical dendrites. This was unique to CA2, as MCU was not significantly enriched in neighboring CA1 distal apical dendrites. MCU-enriched mitochondria in CA2 distal dendrites were more tubular in shape and significantly larger in size compared to mitochondria in CA2 proximal dendrites and CA1 dendrites, whereas there was no significant difference in mitochondria size within CA1 distal dendrites compared to proximal dendrites. Distal dendrites in the hippocampus receive distinct inputs compared to proximal dendrites, demonstrating that mitochondria display cell- and circuit-specific heterogeneity in the hippocampus with a particularly unique subpopulation in CA2 distal dendrites. Overexpression of MCU in CA1 significantly increased MCU fluorescence intensity and apparent MCU-labeled mitochondrial size throughout CA1 apical dendrites, but did not affect the fluorescence intensity or size of COX4-labeled mitochondria in CA1. The increase in MCU-fluorescence after overexpression was preferentially seen in the proximal dendrites compared to the distal dendrites, suggesting a swap in MCU localization within the dendrites of CA1, which was not seen after MCU overexpression in CA2. This suggests that MCU could potentially localize within dendrites to areas of high energy demand, although further studies are needed. Collectively, these data shine light on the molecular and morphological diversity of mitochondria across hippocampal cell types and circuits, and suggest that MCU enrichment in CA2 distal dendrites could potentially be a mechanism for differentially regulating layer-specific synaptic energy demands.

2 | RESULTS

2.1 | MCU is enriched in CA2 distal dendrites and reveals morphological differences across proximal and distal dendrites

In order to assess the heterogeneity of MCU expression across hippocampal circuits, we immunostained hippocampal-containing sections from adult male and female C57bl6/J mice for MCU. Consistent with our transcriptome study (Farris et al., 2019), MCU fluorescence was highly enriched in RGS14-positive CA2 cell bodies and dendrites compared to neighboring CA1 cell bodies and dendrites (Figure 1a–d, two-way repeated measures analysis of variance (RM ANOVA), effect of subregion: $F = 194.1$, $p < .0001$; effect of layer: $F = 21.8$, $p = .0001$; effect of subregion × layer: $F = 43.0$, $p < .0001$). However, within CA2, MCU fluorescence was strikingly enriched in the distal apical dendrites in layer stratum lacunosum moleculare (SLM) compared to the proximal apical dendrites in layer stratum radiatum (SR, Figure 1d, Sidak's multiple comparison test, CA2 SR vs. SLM: $p < .0001$). Compared to principal cell expression, MCU fluorescence was not readily observed in nonneuronal cells present within the neuropil. At both the RNA and protein level, MCU expression is lower in astrocytes than in neurons (Farris et al., 2019; Fecher et al., 2019), suggesting that the bulk of MCU detected in the neuropil is from pyramidal cell expression. The extent of MCU enrichment in CA2 distal dendrites was unique to CA2. There appears to be a slight enrichment of MCU in CA1 SLM, although it was not statistically significant (Figure 1d, CA1 SR vs. SLM: $p = .996$). The distal dendrites of CA2 (SLM) receive layer-specific input from entorhinal cortex layer II, whereas the proximal dendrites (SR) receive input from CA3. These data suggest that there is mitochondrial diversity across hippocampal cell types, and even within dendritic domains of the same cells which reflect distinct hippocampal circuits.

To quantify differences in mitochondrial morphology across the dendritic layers of CA1 and CA2, individual MCU-labeled mitochondria were segmented and quantified to obtain the average mitochondrial area and count for each dendritic layer (see Section 2). Figure S1 includes the data and statistics for all three dendritic layers (stratum oriens [SO], SR, and SLM); however, we focused our analyses on layers SR and SLM, as less is known about CA2 basal dendrite connectivity and plasticity and thus results would be hard to interpret. We found that mitochondrial area varied by subregion and dendritic layer (two-way RM ANOVA, effect of subregion and layer: $p < .0001$). The average MCU-labeled mitochondrial area was significantly greater in SLM compared to SR in CA2, but was not significant in CA1 (Figure 1e, Sidak's multiple comparison test, CA2 SR vs. SLM: $p < .0001$; CA1 SR vs. SLM: $p = .142$). Across both dendritic layers, MCU-labeled mitochondrial area was significantly larger in CA2 than in CA1 (CA1 vs. CA2, SR and SLM both $p < .0001$). Interestingly, the number of mitochondria was significantly less in CA2 than in CA1 for all dendritic layers (Figure 1f; two-way RM ANOVA, effect of subregion: $F = 42.7$, $p = .0006$; Sidek's multiple comparison test, CA1 vs. CA2, SR and SLM both $p < .0001$). There was also an overall

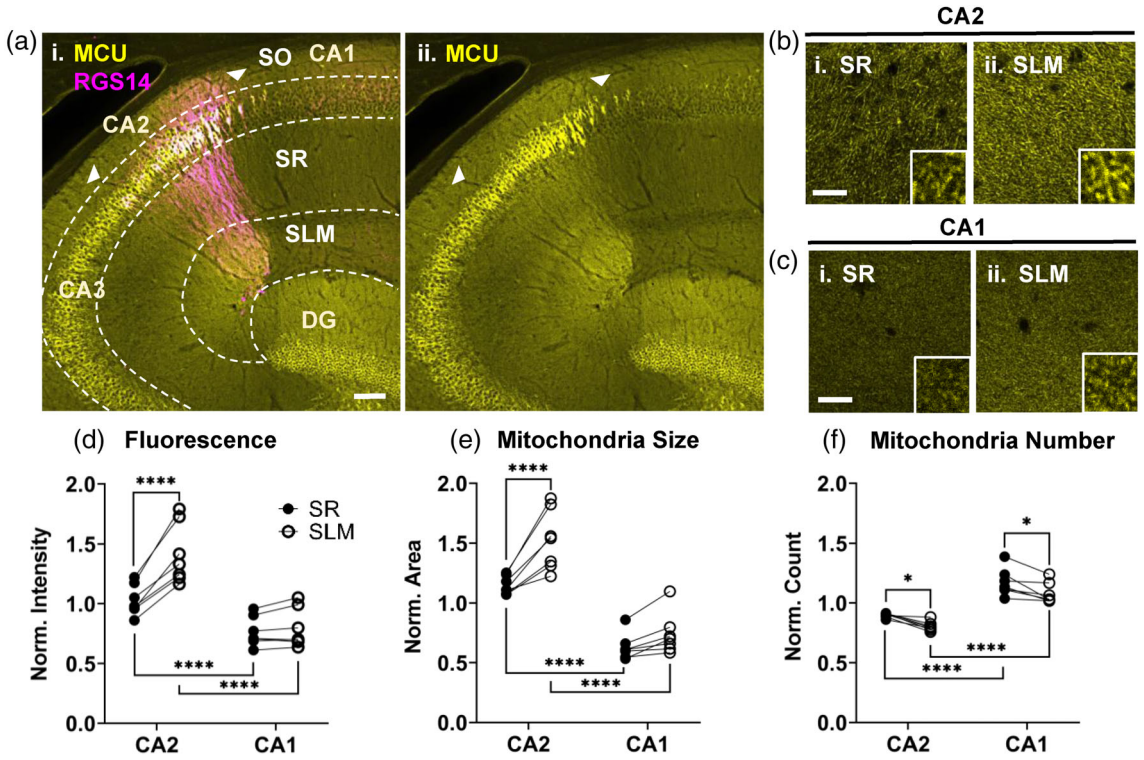

FIGURE 1 Mitochondrial calcium uniporter (MCU)-labeled mitochondria are preferentially enriched in CA2 distal dendrites and larger in size than neighboring mitochondria. (a) (i) 20× epifluorescence tile image of a wild-type hippocampus stained for MCU (yellow) and RGS14 (magenta) with the subregions and dendritic layers labeled. White arrowheads indicate the borders of CA2. (ii) The MCU channel alone. (b) Representative 40× confocal images of MCU staining in SR (i) and SLM (ii) of CA2 in a wild-type mouse. All representative 40× images are from a single Z section. Insets in (b) and (c) are a zoomed 10 × 10 μm crop of the larger image. (c) Representative 40× confocal images of MCU staining in SR (i) and SLM (ii) of CA1 in a wild-type mouse. Images were processed identically to the representative images in (b) for comparison between CA1 and CA2. (d) The mean MCU fluorescence of a representative 100 × 100 μm ROI from SR and SLM of CA1 and CA2. Data were normalized to the overall average. SR (closed circles) and SLM (open circles) of the same animal are paired with lines. Two-way repeated measures analysis of variance (RM ANOVA) with Sidak's post hoc; $n = 7$ animals; 3 hippocampal sections/animal. Overall effect of subregion and layer were significant (subregion: $F = 194.1$, $p \leq .0001$ layer: $F = 21.8$, $p = .0001$; interaction: $F = 43.0$; $p \leq .0001$). (e) The average area of MCU-labeled mitochondria in the same ROIs from (d) Mitochondria were segmented as described in the methods. Data were normalized and plotted the same as in (d). Two-way RM ANOVA with Sidak's post hoc. Overall effect of subregion and layer on area were significant (subregion $F = 102.6$, $p \leq .0001$; layer: $F = 23.1$, $p \leq .0001$, interaction $F = 26.2$ $p \leq .0001$). (f) The average count of MCU-labeled mitochondria from the dataset in (e). Two-way RM ANOVA with Sidak's post hoc. Overall effect of subregion and layer on count were significant (subregion: $F = 42$ 7, $p = .0006$; layer: $F = 17.8$, $p = .0003$, interaction: $F = 11.0$; $p \leq .0019$). SO, stratum oriens; SR, stratum radiatum; SLM, stratum lacunosum moleculare. Sidak's post hoc: $^{*}p < .05$; $^{**}p < .01$; $^{***}p < .001$; $^{****}p < .0001$. Scale for (a) 100 μm; (b) and (c) 20 μm.

effect of layer ($F = 17.8$, $p = .0003$), where we found significantly fewer mitochondria in SLM compared to SR in both CA1 and CA2 (CA1 SR vs. SLM: $p = .026$, CA2 SR vs. SLM: $p = .022$). Thus, mitochondria appear to be generally larger and fewer in the distal dendrites of CA2 compared to the proximal dendrites. MCU-enriched mitochondria in CA2 dendrites are also larger in size and fewer in number compared to mitochondria in CA1 dendrites. These results indicate that CA2 distal dendrites contain a unique subpopulation of mitochondria.

2.2 | COX4 labels a broader but overlapping population of mitochondria than MCU

In addition to MCU, we stained for mitochondria using an antibody against cytochrome c oxidase subunit 4 isoform 1 (COX4), a component of the enzyme complex involved in the terminal step of the mitochondrial electron transport chain. Similar to MCU, COX4 staining was enriched in CA2 cell bodies compared to neighboring CA1 cell bodies (Figure 2a). However, COX4 dendritic staining was more variable and less striking than MCU dendritic staining and thus required a greater number of mice to assess dendritic mitochondrial morphology. This blunted COX4 dendritic expression profile compared to MCU may be due to COX4 expression in nonpyramidal cells within the dendritic laminae (Figure 2a(ii) yellow arrows). Comparing COX4 labeling in the dendritic layers of CA2 and CA1 (Figure 2b,c) revealed small, but significant differences in COX4 fluorescence (Figure 2d, two-way RM ANOVA, effect of layer: $F = 16.9$, $p = .006$) and COX4-labeled mitochondria size (Figure 2e, two-way RM ANOVA, effect of layer: $F = 15.2$, $p = .008$). COX4 fluorescence was increased in SLM compared to SR in both CA2 and CA1 dendrites (Figure 2d, Sidak's multiple comparison test, CA2 SR vs. SLM:

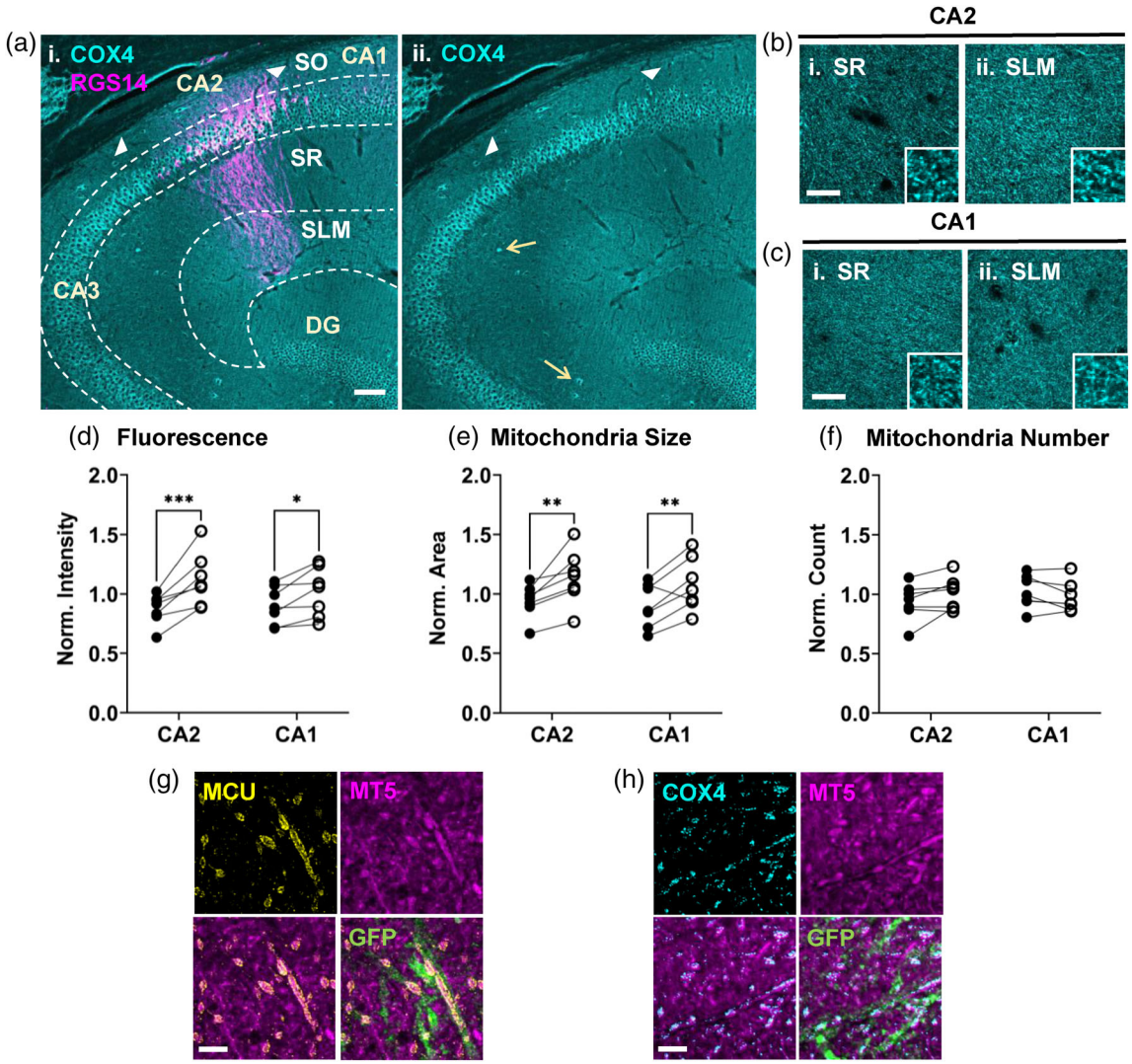

FIGURE 2 COX4 labeling is similarly enriched in CA2 and CA1 distal dendrites. (a) (i) 20× epifluorescence tile image of a wild-type hippocampus stained for COX4 (cyan) and RGS14 (magenta) with the subregions and dendritic layers labeled. White arrowheads indicate the borders of CA2. (ii) The COX4 channel alone. Yellow arrows show examples of COX4 labeling in nonpyramidal cells in the neuropil. (b) Representative 40× confocal Images of COX4 staining in SR (i) and SLM (ii) of CA2 in a wild-type mouse. Insets in (f) and (g) are a zoomed 10 × 10 μm crop of the larger image. (c) Representative 40× confocal images of COX4 staining in SR (i) and SLM (ii) of CA1 in a wild-type mouse. Images in (f) and (g) were processed identically to preserve differences between subregions and dendritic layers. (d) COX4 mean fluorescence of a 100 × 100 μm ROI from SR and SLM of CA1 and CA2 normalized to the overall cohort average. Lines pair SR and SLM of the same animal. Two-way repeated measures analysis of variance (RM ANOVA) with Sidak's post hoc; $n = 7$ animals from two cohorts. Overall effect of subregion was not significant for any metric ($p > .05$), thus subregion comparisons are not shown. Overall effect of layer was significant for fluorescence ($F = 13.4$, $p = .011$). (e) Mean area of COX4-labeled mitochondria in the same ROIs in (d). Mitochondria were segmented the same as in Figure 1 and data were normalized to the overall cohort average. Two-way RM ANOVA with Sidak's post hoc. Overall effect of layer on area was significant ($F = 15.5$, $p = .008$). (f) Mean count of COX4-labeled mitochondria from the same dataset as (e). Two-way RM ANOVA with Sidak's post hoc. The overall effect of layer and subregion on mitochondria count were not significant ($p > .05$). (g) Representative ProExM images of MCU (yellow) and MT-5 (magenta) in CA2 SLM. Bottom panels show the overlay of both channels (left) and an overlay with GFP+ CA2 distal dendrites (right). (h) Representative ProExM images of COX4 staining (cyan) and MT-5 staining (magenta) in CA2 SLM. An ROI was chosen which had a similar amount of MT-5 and GFP staining as in (g) for comparison. Sidak's post hoc: *$p < .05$; **$p < .01$; *** $p < .001$. Scale for (a) 100 μm; (b) and (c) 20 μm; (g)–(h) 3 μm (ExM adj.).

$p = .0003$; CA1 SR vs. SLM: $p = .019$). Similarly, COX4-labeled mitochondrial area was increased in SLM compared to SR in both CA2 and CA1 (Figure 2e, Sidak's multiple comparison test, CA2 SR vs. SLM: $p = .002$; CA1 SR vs. SLM: $p = .004$). Unlike with MCU-labeled mitochondria, there was no statistical difference in COX4 fluorescence or COX4-labeled mitochondrial area between CA2 and CA1 dendrites (Figure 2d,e, two-way RM ANOVA, effect of subregion: $p > .05$ for fluorescence and area). There was also no significant difference in the number of COX4-labeled mitochondria in CA2 versus CA1, or across dendritic layers (Figure 2f, two-way RM ANOVA, effect of subregion and layer: $p > .05$). In sum, COX4-labeled mitochondria show no significant differences across subregions CA1 and CA2, but show consistent increases in fluorescence and mitochondrial area in distal dendrites compared to proximal dendrites. Thus, the selective

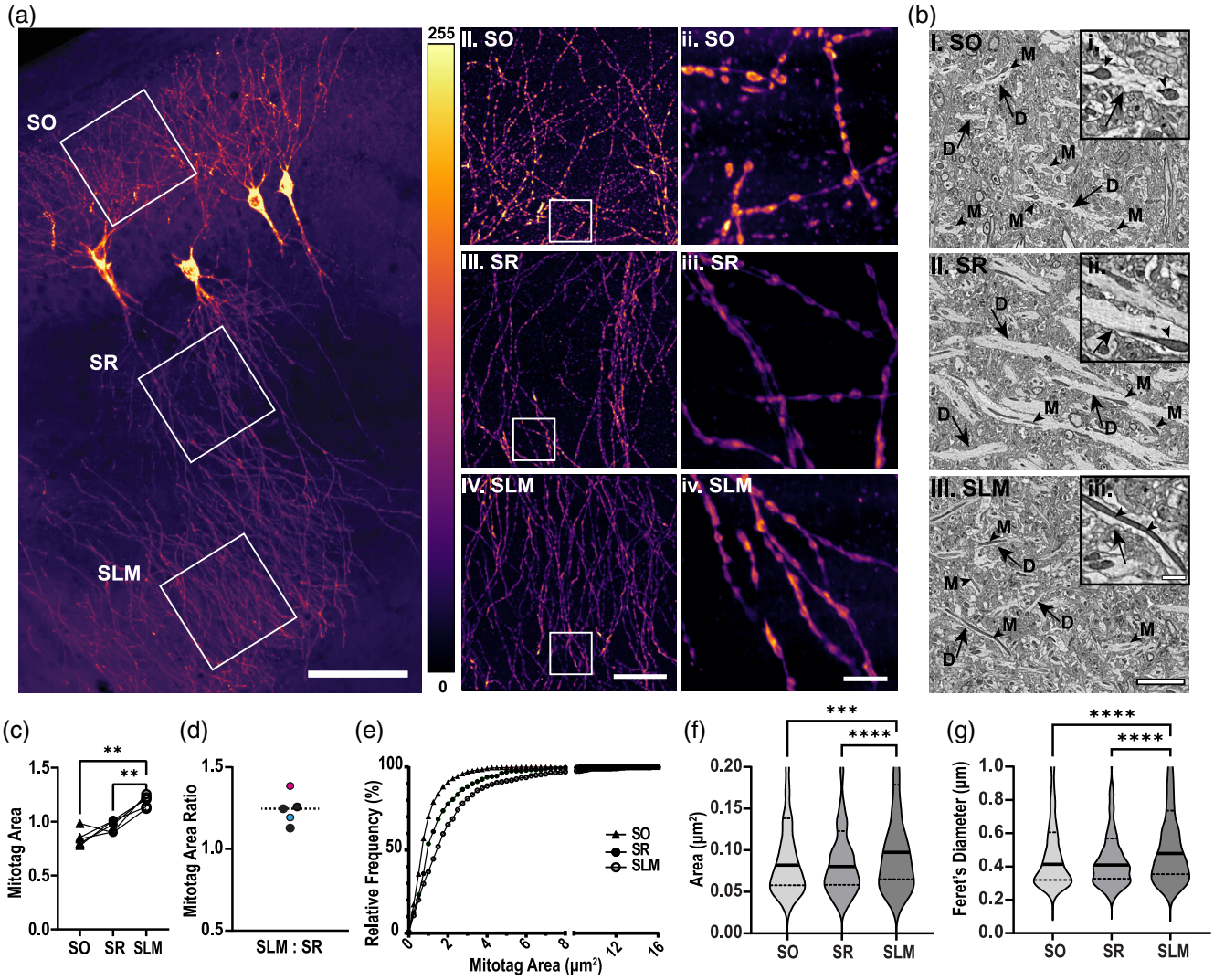

FIGURE 3 Super resolution imaging and electron microscopy confirm CA2 layer-specific differences in dendritic mitochondrial morphology. (a) (i) Representative 20× confocal image of sparse CA2 neuron Mitotag labeling of mitochondria. ROIs (white box) within the 20× image indicate the selection for 60× (ii) SO, (iii) SR, and (iv) SLM representative images. ROI (white box) within 60× images is representative of 10 × 10 μm^2 4× super-resolution images of Mitotag labeled mitochondria in individual (ii) SO, (iii) SR, and (iv) SLM dendritic branches. (b) Representative electron micrographs of (i) SO, (ii), SR, and (iii) SLM dendrites. Examples of mitochondria (arrowheads) within dendrite (arrows) cross sections are indicated. (c) Median Mitotag-labeled mitochondrial area in CA2 SO, SR, and SLM dendritic layers. Data are normalized to the average area per mouse with lines connecting SO, SR, and SLM per mouse. Mitochondrial size was significantly increased within the SLM layers compared to both SO and SR in the CA2 (one-way repeated measures analysis of variance [RM ANOVA]: $F = 23.47$, $p = .0014$, Tukey's multiple comparison test; $n = 5$ mice, 4–7 hippocampus sections/animal). (d) Ratio of the median mitochondrial area between SLM and SR layers in (c). Color-filled data points represent the mice selected for representative images (a: blue; e: pink). (e) Percent relative frequency plot of individual mitochondrial areas from CA2 SO, SR, and SLM from one representative section from the mouse labeled in pink in (d). (f) Violin plots of mitochondria area in scanning electron micrographs of CA2 SO, SR, and SLM, measured in 100 μm^2 ROIs. Kruskal–Wallis test with Dunn's correction. SO $n = 573$, SR $n = 475$, SLM $n = 559$ from $n = 3$ mice. Solid line = median; dashed line = upper and lower quartiles. (g) Violin plots of mitochondria Feret's diameter in the same scanning electron micrographs of CA2 SO, SR, and SLM as in (f). Kruskal–Wallis test with Dunn's correction. SO, stratum oriens; SR, stratum radiatum; SLM, stratum lacunosum moleculare. Post hoc comparisons: *p < .05; **p < .01; ***p < .001; ***p < .0001. Scale (ai) 100 μm, (aiv) 25 μm, (aiv, b(iii)) 5 μm, and (Bii&$$;) 1 μm.

enrichment of MCU in the distal dendrites of CA2 compared to CA1 appears to be unique, suggesting the mitochondria there are molecularly distinct.

To test the possibility that MCU is labeling a subpopulation of COX4-labeled mitochondria, we acquired super resolution images of MCU- (Figure 2g) and COX4- (Figure 2h) labeled mitochondria in CA2 SLM alongside a novel pan-mitochondrial matrix marker MT-5 (Kalyuzhny et al., 2021). We used protein retention expansion microscopy (ProExM) to visualize densely packed mitochondria (Campbell et al., 2021). In order to compare MCU and COX4 labeling across similar mitochondrial populations, we used ProExM images with similar MT-5 and CA2 SLM dendrite content. Although MCU and COX4 both labeled the inner mitochondrial membrane surrounding MT-5 labeled mitochondrial matrix, MCU-labeled mitochondria were qualitatively larger and less numerous than COX4-labeled mitochondria. This suggests that MCU may label a subset of the mitochondrial

population labeled with COX4, perhaps only mitochondria in CA2 dendrites versus mitochondria from multiple cell populations within the neuropil.

2.3 | Genetically labeled mitochondria in CA2 distal dendrites are increased in size relative to the proximal dendrites

To confirm the difference in mitochondrial mass between the proximal and distal dendrites of CA2, we used a genetic strategy to sparsely label CA2 neurons with GFP-tagged mitochondria. We crossed Mitotag mice (Fecher et al., 2019) to a tamoxifen-inducible CA2-specific cre line (Amigo2-iCreERT2; Alexander et al., 2018), which allowed for mitochondria to be resolved in individual CA2 neuron dendrites (Figure 3a). Consistent with our MCU immunolabeling, mitochondria size varied by CA2 dendrite layer with smaller, punctate mitochondria in SO compared to enlarged, tubular mitochondria in SLM, with SR mitochondria sized in between. Similar results were seen in scanning electron micrographs (SEM, Figure 3b), where mitochondria in CA2 SLM were larger and more tubular than mitochondria in SO or SR. The median area of Mitotag-labeled mitochondria in SLM was statistically greater than Mitotag-labeled mitochondria in both SO and SR (Figure 3c, one-way RM ANOVA, $F = 23.47$, $p = .0014$, Tukey's multiple comparison test, SO vs. SLM: $p = .009$; SR vs. SLM: $p = .007$). The ratio of median mitochondrial areas for SLM to SR was consistently above 1.0 across mice (Figure 3e, average SLM:SR ratio = 1.24 ± 0.04 SEM, $n = 5$ mice) and the relative frequency curve for individual mitochondrial areas in SLM was shifted to the right compared to individual mitochondrial areas in SO and SR (Figure 3e). Consistent with this, quantification of mitochondria in electron micrographs from the three layers showed mitochondria in SLM had significantly larger areas and diameters compared to mitochondria in either SO or SR (Figure 3f,e; Kruskal–Wallis test; SO $n = 573$ mitochondria, SR $n = 475$, SLM $n = 559$ from $n = 3$ mice. Area: $F = 24.7$, $p < .0001$; Feret's diameter: $F = 29.9$, $p < .0001$). Collectively, these findings indicate that layer-specific differences in mitochondrial morphology are not a result of enriched MCU or COX4 antibody staining creating the relative appearance of larger mitochondria.

2.4 | MCU overexpression changes the localization of MCU in CA1 dendrites

Although the exact role of MCU in regulating mitochondrial function is still being explored, it has been shown that calcium influx into the mitochondrial matrix stimulates ATP production via the TCA cycle (Llorente-Folch et al., 2015; Wescott et al., 2019), causes morphological changes by inducing mitochondrial fragmentation via fission (Han et al., 2008), and regulates the transport of mitochondria and the localization of mitochondria at active synapses (Wang & Schwarz, 2009). Based on our findings that MCU expression correlates with increased mitochondrial size in the distal dendrites of CA2, we next asked whether increasing MCU expression can increase mitochondrial size or influence the apparent enrichment of MCU in the distal dendrites of neighboring CA1. To test this, we used adeno-associated viral vectors (AAVs) to overexpress MCU or GFP in CA1 neurons, which normally have fourfold less *Mcu* expression than CA2 neurons (Farris et al., 2019). CA1 was stereotaxically targeted in wild-type mice to infuse either AAV-MCU (AAV9-hSYN1-mMCU-2A-GFP-WPRE) or AAV-GFP (AAV9-hSYN1-eGFP) as a control. We then immunostained for MCU and GFP and quantified the mean MCU fluorescence and the size and number of MCU-labeled mitochondria in SO, SR and SLM of CA1. MCU expression was about ~4.5-fold greater overall in the AAV-MCU treated mice than the control AAV-GFP treated mice (Figure 4a,b). MCU overexpression in CA1 significantly increased MCU fluorescence in CA1 SR and SLM (Figure 4c; two-way RM ANOVA, effect of AAV: $F = 124.4$, $p \leq .0001$) and resulted in apparently larger MCU-labeled mitochondria measured in CA1 dendrites compared to GFP control mice (Figure 4d; two-way RM ANOVA, effect of AAV: $F = 124.4$, $p \leq .0001$). However, the effect of MCU overexpression was greater in CA1 SR compared to SLM for MCU fluorescence (Figure 4c, Sidak multiple comparisons; $p = .002$) and apparent mitochondrial size (Figure 4D; Sidak multiple comparisons, $p = .005$) (Figure S2). This indicates that, in contrast to CA2 dendrites where MCU expression is enriched in mitochondria in distal dendrites, MCU overexpression in CA1 preferentially causes MCU enrichment in proximal dendrites compared to distal dendrites. Importantly, an increase in fluorescence or mitochondrial area was not seen with another pan mitochondrial marker, COX4, in the same tissue (Figure 4e,f). There was no effect of AAV-treatment for COX4 fluorescence (Figure 4g; $F = 0.02$; $p = .89$), COX4-labeled mitochondrial size (Figure 4h; $F = 0.28$; $p = .61$) or number (Figure S2; $F = 0.28$; $p = .61$). Unlike with MCU-labeled mitochondria, MCU overexpression did not alter the distal enrichment of COX4-labeled mitochondria relative to the proximal dendrites. Our results suggest that MCU overexpression can alter the localization of MCU itself without a measurable increase in overall mitochondrial size or number. The apparent size increase measured in MCU-labeled mitochondria in AAV-MCU mice was likely a result of increased MCU fluorescence. Interestingly, in a handful of MCU-AAV mice where CA2 was also transduced, the preferential enrichment of MCU in the proximal dendrites that was seen in CA1 was not seen in CA2 (Figure S3). Again, suggesting that distinct hippocampal circuits are differentially regulated by diverse pools of mitochondria.

3 | DISCUSSION

The goal of this study was to investigate mitochondrial heterogeneity in the mouse hippocampus. Focusing on the enrichment of MCU in area CA2, we unexpectedly uncovered that MCU expression is preferentially enriched in CA2 distal apical dendrites, precisely where CA2 neurons receive layer-specific input from entorhinal cortex II, a circuit

recently shown to carry social information to CA2 (Dang et al., 2022; Lopez-Rojas et al., 2022). This striking enrichment of MCU in CA2 distal dendrites compared to CA2 proximal dendrites and neighboring CA1 dendrites is not seen with another mitochondrial marker, COX4, suggesting that mitochondria in CA2 distal dendrites have a unique molecular expression profile. We found that the ratio of MCU fluorescence in SLM:SR was highest in CA2 (1.72 ± 0.16), followed by CA1 (1.19 ± 0.13) and CA3 (1.10 ± 0.06). While CA3 was not included in

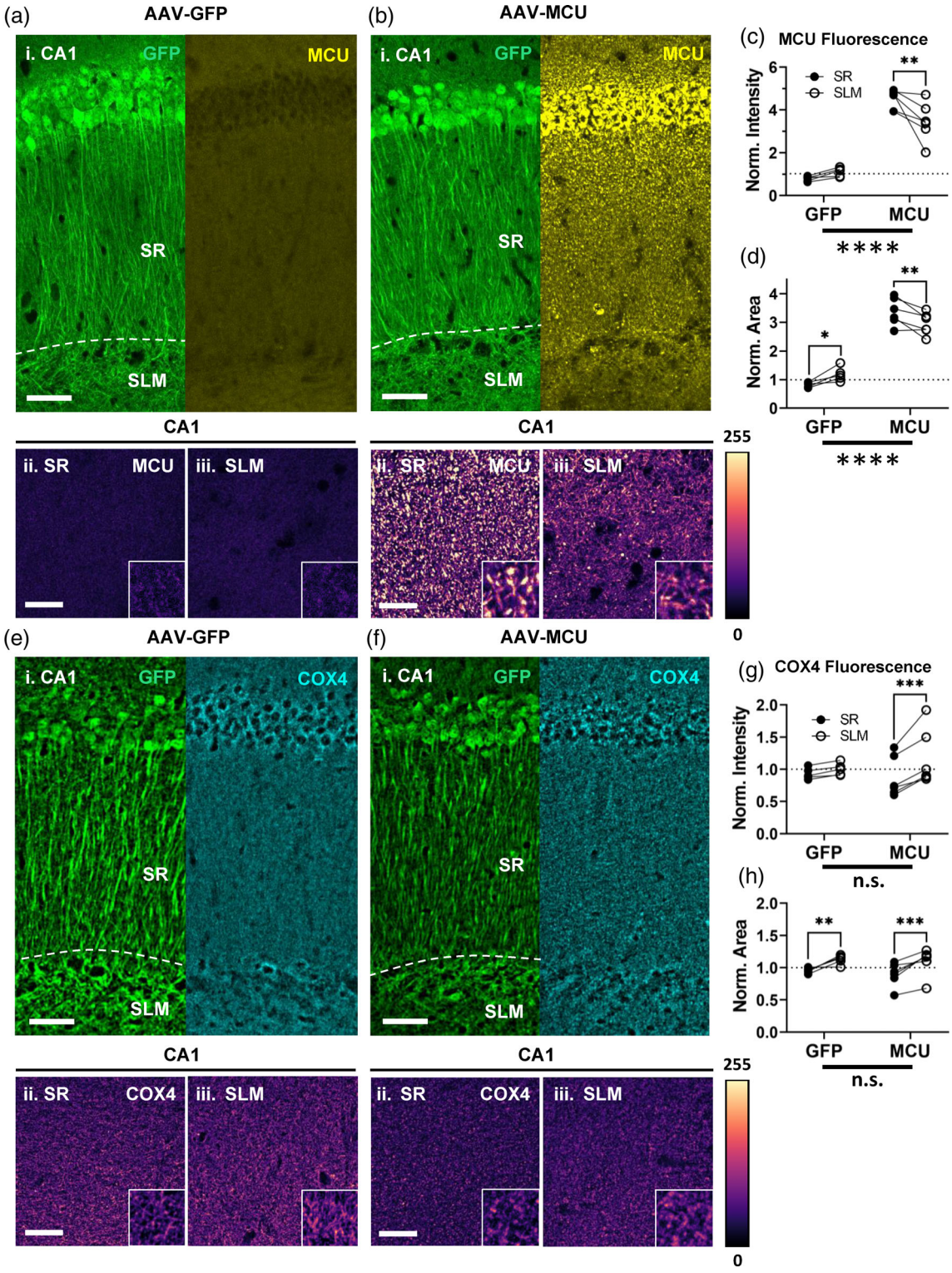

FIGURE 4 Legend on next page.

our analyses, we previously showed with RNA sequencing that the transcriptional profile of CA3 neurons is more similar to CA2 neurons than CA1 and DG (Farris et al., 2019). We and others have shown that *Mcu* expression is about 2-fold higher in CA3 than in CA1 (Farris et al., 2019; Márkus et al., 2016). Consistent with this, we saw that the MCU fluorescence in CA2 cell bodies was 1.6-fold higher than CA1, and CA3 cell bodies were 1.4-fold higher than CA1. However, despite their similarities, CA3 neurons did not display the same asymmetric distribution of MCU expression across SR and SLM seen in CA2 neurons, as the ratio of MCU fluorescence in SLM to SR was near 1. We further found that MCU-enriched mitochondria in CA2 distal dendrites are larger and more tubular compared with mitochondria in CA2 proximal dendrites and CA1 apical dendrites. The increased mitochondrial size in the distal dendrites of CA2 was not limited to MCU-labeled mitochondria, as this was seen in COX4-labeled mitochondria, as well as in genetically labeled mitochondria and mitochondria in electron micrographs. Studies in cultured hippocampal neurons have demonstrated that elongated mitochondria in axons can take up more calcium, suggesting a direct connection between mitochondrial morphology and function (Lewis et al., 2018). Other studies suggest that MCU is localized to specific subdomains of the inner mitochondrial membrane, where calcium concentrations are highest (Wang et al., 2019). This is consistent with our finding that MCU overexpression in CA1 enriches MCU expression preferentially in the proximal dendrites of CA1, which are more efficient at triggering somatic excitatory postsynaptic currents (EPSCs; Srinivas et al., 2017) and are more plastic than CA1 distal dendrites (Sajikumar & Korte, 2011), which collectively could produce higher intracellular calcium levels. While further studies are required to establish the functional role of MCU enrichment in CA2 distal dendrites, our results revealed unexpected mitochondrial diversity across hippocampal subregions and compartments. In particular, we identified a molecularly and structurally distinct subpopulation of mitochondria in CA2 distal dendrites that could potentially have implications for regulating local calcium dynamics and thereby influence circuit-specific forms of plasticity.

3.1 | Evidence for a distinct subpopulation of mitochondria in CA2 distal dendrites

Several lines of evidence support the finding that CA2 distal dendrites harbor a unique pool of mitochondria. (1) MCU is selectively enriched in mitochondria in CA2 distal dendrites compared to neighboring subregions. (2) MCU-labeled mitochondria are visibly and quantitatively larger in CA2 distal dendrites compared to CA2 proximal dendrites and CA1 apical dendrites, although this could be attributed to an increase in MCU expression in CA2 distal dendrites. (3) Quantification of GFP-tagged mitochondria in sparsely labeled CA2 dendrites closely mirrored the results from MCU-labeled mitochondria in that distal dendrites harbored larger mitochondria than proximal and basal dendrites. (4) Quantification of electron micrographs in each dendritic layer of CA2 confirmed the results from the other methods, that mitochondria in CA2 distal dendrites are larger and more tubular than mitochondria in CA2 proximal and basal dendrites. Interestingly, staining with another mitochondrial protein, COX4, showed similar, albeit smaller, differences in fluorescence and mitochondrial size between CA2 proximal and distal dendrites; however, we did not detect COX4-labeled mitochondrial differences between CA1 and CA2, as strikingly seen with MCU-labeled mitochondria. We noted that COX4-labeled mitochondria appear to be more numerous than MCU-labeled mitochondria across comparative populations, and that COX4 labels mitochondria in non-pyramidal cells within the neuropil, whereas MCU in the hippocampus is, for the most part, limited to

FIGURE 4 Mitochondrial calcium uniporter (MCU) preferentially localizes to the proximal dendrites of CA1 after MCU overexpression. (a) (i) Representative 20× epifluorescence image of GFP (left) and MCU (right) staining in CA1 of an AAV-GFP treated mouse. Bottom: Representative 40× confocal images of MCU staining in SR (ii) and SLM (iii) of CA1 in a AAV-GFP treated mouse. Inset is a zoomed 10 × 10 μm crop. A LUT was applied to highlight the dynamic range of intensity. (b) (i) Representative 20× epifluorescence image of GFP (left) and MCU (right) staining in CA1 of an AAV-MCU treated mouse. Bottom: Representative 40× confocal images of MCU staining in SR (ii) and SLM (iii) of CA1 in an AAV-MCU treated mouse. (a) and (b) were processed the same to maintain differences between AAV-MCU and AAV-GFP mice. (c) Mean MCU fluorescence of a 100 × 100 μm ROI from SR and SLM of AAV-GFP and AAV-MCU mice normalized to GFP control average. $n = 5$ AAV-GFP and 6 AAV-MCU mice. Two-way repeated measures analysis of variance (RM ANOVA) with Sidak's post hoc comparing dendritic layers. Overall effect of AAV treatment and layer were significant (treatment: $F = 113.4$, $p \leq .0001$; Layer: $F = 4.81$, $p = .021$). See Table S1 for post hoc comparisons. (d) Mean MCU-labeled mitochondrial area in SR and SLM of the AAV-MCU and AAV-GFP mice normalized to GFP control average. Two-way RM ANOVA with Sidak's post hoc. Overall effect of treatment and layer were significant (treatment: $F = 124.4$, $p < .0001$, layer; $F = 3.84$, $p = .041$). (e) (i) Representative 20× epifluorescence image of GFP (left) and COX4 (right) staining in CA1 of an AAV-GFP treated mouse. Bottom: Representative 63× epifluorescence images of COX4 staining in SR (ii) and SLM (iii) of CA1 in a AAV-GFP treated mouse. Inset is a zoomed 10 × 10 μm crop. (f) (i) Representative 20× epifluorescence image of GFP (left) and COX4 (right) staining in CA1 of an AAV-MCU treated mouse Bottom: Representative 63× epifluorescence images of COX4 staining in SR (ii) and SLM (iii) of CA1 in an AAV-MCU treated mouse. (e) and (f) were processed the same to maintain differences between AAV-MCU and AAV-GFP mice. (g) Mean COX4 fluorescence of a 100 × 100 μm ROI from SR and SLM of the same AAV-GFP and AAV-MCU mice in (c) and (d) normalized to GFP control average. $n = 5$ AAV-GFP and 6 AAV-MCU mice Two-way RM ANOVA with Sidak's post hoc comparing dendritic layers. Overall effect of AAV-treatment was not significant ($F = 0.02$, $p = .89$). Overall effect of layer was significant ($F = 10.4$, $p = 001$). (h) Mean COX4-labeled mitochondrial area in SR and SLM of the AAV-MCU and AAV-GFP mice normalized to GFP control average. Two-way RM ANOVA with Sidak's post hoc. Overall effect of AAV-treatment was not significant ($F = 0.28$, $p = .61$). Overall effect of layer was significant ($F = 28.9$, $p \leq .0001$). SR, stratum radiatum; SLM, stratum lacunosum moleculare. Sidak's post hoc: $^{*}p < .05$; $^{**}p < .01$; $^{***}p < .001$. Scale for (a) and (b) (i) 50 μm; scale for (a) and (b)(ii–iii) 20 μm, scale for (g) 3 μm, inset = 1 μm (ExM adj.).

mitochondria in pyramidal neurons. At the level of RNA, we did not find *Mcu* expression in glia (Farris et al., 2019), and others have shown with proteomic profiling of the cerebellum that MCU is low in astrocytes compared to excitatory principal neurons (Fecher et al., 2019). It is also been shown that calcium influx into astrocytic mitochondria does not require MCU (Huntington & Srinivasan, 2021), suggesting that glial cells may have an MCU-independent mechanism for calcium influx into the mitochondria. Thus, COX4-labeling likely includes a broader population of mitochondria beyond mitochondria in CA2 or CA1 dendrites, of which MCU may be labeling a subset of mitochondria that partially overlap with COX4-labeled mitochondria. Thus, while considerable data support layer-specific mitochondrial differences within CA2 (i.e., SR vs. SLM), thus far, the only confirmed *difference* uncovered between mitochondria in CA1 and CA2 dendrites is the amount of MCU labeling, which could influence the other metrics. Further studies are required to incisively elucidate whether MCU-enriched mitochondria in CA2 distal dendrites are molecularly distinct from neighboring mitochondria in other ways (i.e., express other unique mitochondrial proteins). Moreover, further studies are needed to firmly establish whether mitochondria in CA2 are morphologically distinct from mitochondria in CA1 or whether they appear as such due to their greater MCU expression.

3.2 | Potential functional roles for a distinct subpopulation of mitochondria in CA2 distal dendrites

There are at least two possible reasons for why mitochondria are different in CA2 distal apical dendrites. First, the CA regions receive dendritic layer-specific inputs which have different efficacies for generating somatic responses. Inputs that are more proximal to the soma typically cause a larger somatic EPSC; however, ECII inputs onto the distal dendrites of CA2 drive an unusually robust response in CA2 neurons, 5- to 6-fold larger EPSCs than those evoked from ECIII inputs onto CA1 neurons (Srinivas et al., 2017, but see also Sun et al., 2021). This enhanced efficacy is the result of unique synaptic and dendritic properties in CA2 SLM (Srinivas et al., 2017; Sun et al., 2014), including almost three times as many glutamatergic synapses in CA2 SLM than in CA1 SLM (Srinivas et al., 2017), although there is heterogeneity in CA2 dendritic SLM morphology (Helton et al., 2019). Moreover, there is an asymmetrical gradient of innervation from ECII, with the lateral entorhinal cortex II (LECII) axons covering a larger area more distal from the soma than the medial entorhinal cortex II axons (MECII) (Steward, 1976). This is consistent with the asymmetric pattern of MCU-labeled mitochondrial morphology in CA2 dendrites. Notably, input from the LECII, but not the MECII, carries social information relevant to social recognition memory (Lopez-Rojas et al., 2022). Taken together, CA2 SLM may have higher expression of MCU and, potentially, greater mitochondrial mass than CA1 SLM in order to metabolically support more numerous and more active synapses. A relationship between neuronal activity and MCU activation is just beginning to be fleshed out. A recent study found that increased action potential firing in cortical and hippocampal pyramidal neurons in acute slices led to an increase in MCU activation and mitochondrial calcium influx, which was blocked by application of the MCU inhibitor Ru360 (Groten & MacVicar, 2022). This effect on mitochondrial calcium uptake scaled with action potential firing frequency and resulted in increased mitochondrial metabolism. Interestingly, the coupling of activity to mitochondrial calcium uptake differed between pyramidal neurons in CA1 of hippocampus and the cortex, suggesting that MCU is differentially regulated by activity in different cell types (Groten & MacVicar, 2022). In the cerebellum, higher expression of MCU in granule cells compared to Purkinje cells and astrocytes also correlated with greater mitochondrial calcium uptake and buffering capacity (Fecher et al., 2019), which is associated with an increase in ATP production (Wescott et al., 2019). Future studies will be needed to expand on whether there are layer-specific differences in metabolic demand that depend on MCU.

Second, the proximal and distal circuits within CA2 dendrites also have distinct plasticity profiles. Synapses from CA3 onto CA2 SR are known to be resistant to long-term potentiation (LTP, Zhao et al., 2007; Simons et al., 2009), while synapses in CA2 SLM from the entorhinal cortex readily express LTP (Chevaleyre & Siegelbaum, 2010). As a result, the more plastic synapses in CA2 SLM may have a higher metabolic demand than the less plastic synapses in CA2 SR. It is known that mitochondria are actively recruited to the presynapse, where it is thought that they locally regulate ATP and cytoplasmic calcium to support synaptic transmission (Chang et al., 2006). In axons, MICU3, a brain-specific regulator of MCU, is necessary for activity-dependent mitochondrial calcium uptake and ATP synthesis to fuel synaptic transmission (Ashrafi et al., 2020). At the post-synapse, repeated stimulation of cultured hippocampal neurons induces mitochondria to invade enlarged spines in an NMDA-dependent manner (Li et al., 2004), which in theory could support a plasticity-induced increase in energetic demand. Studies have further shown that dendritic mitochondria in cultured neurons serve as a local energy source to fuel local translation-dependent changes at synapses during plasticity (Rangaraju et al., 2019). Similarly, the tubular, MCU-enriched mitochondria in the distal dendrites of CA2 could support the increased propensity for plasticity at these synapses. Given the role of MCU in calcium buffering and homeostasis, it is also possible that MCU plays a more direct role in LTP by regulating cytoplasmic calcium levels. We have previously shown that pharmacological blockade of mitochondrial calcium influx through MCU with Ru360 results in changes to the plasticity-resistant profile of CA2 SR synapses (Farris et al., 2019). However, it remains to be tested how MCU-enriched CA2 SLM synapses respond to MCU blockade or MCU knockout. Other studies have shown that MCU overexpression can increase mitochondrial calcium uptake after NMDA receptor activation (Qiu et al., 2013). In addition, mitochondrial fission, which is regulated by calcium influx into mitochondria, is required for structural LTP in CA1 (Divakaruni et al., 2018). However, the exact role MCU might be playing in regulating the plasticity at CA2 SLM synapses is an open question.

3.3 | Limitations

We acknowledge that the present study has several limitations that raise important caveats to our conclusions. One limitation is that, for

all the analyses except Figure 3 where we looked at genetically tagged mitochondria and mitochondrial ultrastructure in CA2, the quantification of mitochondrial area was based on immunofluorescence. Therefore, greater staining intensity, or differences in the quality of antibody labeling could contribute to differences in apparent mitochondrial size. However, the differences in mitochondrial size uncovered between the distal and proximal dendrites of CA2 were corroborated by two independent methods, a genetic mitochondrial tag and EM ultrastructure. Independent validation has not yet been done comparing mitochondrial sizes in CA1 and CA2. Although we measured a general increase in size in CA2 mitochondria compared to CA1 mitochondria with MCU (Figure 1e) in both SR and SLM, a size difference was not seen between COX4-labeled mitochondria in CA1 and CA2 (Figure 2e). Thus, the higher expression of MCU in CA2 relative to CA1 could be contributing to the measured size differences. However, CA2 contains twice as much mitochondrial DNA as CA1 (Farris et al., 2019), which is consistent with CA2 containing greater mitochondrial content than CA1, although it is not clear whether a difference in mitochondrial content or abundance would also be reflected by layer specific differences. Additional studies with higher resolution methods are needed to confirm whether mitochondria are generally larger in CA2 dendrites compared to CA1 dendrites.

Similarly, after MCU overexpression, MCU-labeled mitochondria appeared to be increased in size compared to controls; however, a size difference was not detected in COX4-labeled mitochondria between the AAV-MCU and the AAV-GFP conditions (Figure 4h). Thus, the size difference we measured in Figure 4d was likely due to the overexpression of MCU increasing MCU fluorescence and not a true increase in mitochondrial mass. In addition, a 4-fold overexpression of MCU could lead to abnormal mitochondrial morphology. Although we found that the size of COX4-labeled mitochondria did not change after MCU overexpression, we note that COX4-labeled mitochondria looked qualitatively different after MCU overexpression compared to wild-type. Overexpression of MCU may be changing mitochondria in ways not detected by our methods. More sensitive methods, such as quantification of EM ultrastructure or functional studies may glean further insight. It remains an open question whether MCU expression can directly regulate mitochondrial size, but our data suggest that MCU can be differentially localized within dendritic mitochondria in a circuit-specific manner.

4 | METHODS

4.1 | Animals

All experiments were performed on adult male and female wild type mice on a C57BL/6J background. To generate inducible, CA2-specific Mitotag mice for Figure 3, Amigo2-iCreERT2 mice (Alexander et al., 2018) were crossed with homozygous Mitotag mice (Rosa26-CAG-LSL-GFP-OMM; Jax #: 032675; Fecher et al., 2019). Heterozygous Mitotag$^{fl/WT}$; Amigo2-iCre$^{+/-}$ male and female mice were intraperitoneally injected with Tamoxifen (100–150 mg/kg) over five consecutive days between postnatal (P) ages P26-61 and euthanized 4–12 days post injection to vary the levels of CA2 neuron labeling for experiments in Figure 3. Mice were group-housed under a 12:12 light/dark cycle with access to food and water ad libitum. All procedures were approved by the Animal Care and Use Committee of Virginia Tech.

4.2 | AAV stereotaxic infusions

Prior to surgery, mice received an intraperitoneal (i.p.) injection of ketamine/dexdomitor cocktail (ket 100 mg/kg; dex 0.5 mg/kg) for anesthesia. Mice were put on an absorbent pad and eyes covered with ophthalmic lubricant before being positioned into a stereotaxic apparatus with ear bars. The hair around the incision site was trimmed with electric clippers, and the incision area cleaned with 3 cycles of alternating betadine and 70% alcohol. After clearing the skull, a drill was used to make a unilateral burr hole targeting CA1 of the hippocampus (−2.1 AP; −1.4 ML; −1.4 DV). Using a glass pipette attached to a syringe pump, 0.1–0.3 µL of AAV-MCU (AAV9-hSYN-mMCU-2A-GFP-WPRE, Vector Biolabs, AAV-254662) or AAV-GFP (AAV9-hSYN1-eGFP, Vector Biolabs, VB1107) was infused into the hippocampus at a flow rate of 100 nL/min. After 5 min, the glass pipette was slowly retracted at a rate of 0.5 mm/min and the incision was closed with surgical glue. Mice were given a subcutaneous injection of buprenorphine (0.05–0.5 mg/kg) for analgesia and an IP injection of antisedan (atipamezole, 1 mg/kg) and allowed to recover on a heating pad until ambulatory. Two weeks after infusion, mice were given an overdose of sodium pentobarbital (150 mg/kg) and transcardially perfused with 4% paraformaldehyde then processed for immunohistochemistry as described below.

Due to the potential for MCU overexpression to cause cell death (Granatiero et al., 2019), we immunostained AAV treated sections for MAP2 and GFAP. We found no evidence of cell death or gliosis in CA1 of the AAV-MCU or AAV-GFP infused mice as was seen in mouse cortical neurons, but not zebrafish retina cone photoreceptors (Hutto et al., 2020). When targeting CA2 neurons (Figure S3), AAVs were diluted 1:10 before infusion as direct infusion led to gliosis and loss of GFP expression in CA2 in a subset of mice. Note that CA2 neurons have an enhanced tropism for AAVs (Alexander et al., 2022) that likely led to a pathological level of MCU expression. Taken together, we presume this is an indication that different cell types have various capacities for MCU expression and/or mitochondrial calcium influx based intrinsic or extrinsic factors related to calcium signaling.

4.3 | Immunofluorescence

Mice were anesthetized with 150 mg/kg sodium pentobarbital and transcardially perfused with 15 mL of ice-cold 4% paraformaldehyde. Brains were dissected and post-fixed for at least 24 h before sectioning 40–50 µm thick sections in the horizontal plane on a vibratome (Leica VT1000S). All brain sections immunostained with MCU or

COX4 underwent antigen retrieval by boiling free floating sections for 4–5 min in 1 mL of nanopure water, followed by a permeabilization step in 0.03% Triton-100x for 15 min at room temperature. All sections were then washed in PBS and blocked for 30–60 min in 5% normal goat serum (NGS)/0.03% Triton-100x. Sections were incubated overnight (18–24 h) with primary antibodies: rabbit-anti-MCU (1:500, Novus Cat# NBP2-76948, RRID:AB_2924913), rabbit-anti-COX4 (1:500, SySy 298003), chicken-anti-GFP antibody (1:500, Abcam ab13970), or a chicken-anti-RFP antibody (1:500, SySy 409-006) for any tissue containing the respective reporter. In some cases where CA2 was not labeled genetically, a mouse-anti-RGS14 antibody (1:500, NeuroMab 75–170), rabbit-anti-NECAB2 (1:500, Novus NBP2-84002), or rabbit-anti-PCP4 (1:1000, Invitrogen PA5-52209) was used to label CA2. After several rinses in PBS-T (0.03% Triton-100x), sections were given a quick second block (10–20 min) before incubating in secondary antibodies for 2 h at room temperature. The following secondary antibodies were diluted 1:500 in blocking solution: Invitrogen goat-anti-mouse-488 A11029, goat-anti-chicken-488 A11039, goat-anti-rabbit-546 A11035, or Sigma goat-anti-mouse-633 SAB4600141. Prior to imaging, sections were washed in PBS-T and mounted under Prolong gold fluorescence media with 4′,6-diamidino-2-phenylindole (DAPI) (Invitrogen, P36931).

4.4 | Image acquisition and processing

Images were acquired on an inverted Zeiss 700 confocal microscope equipped with a motorized stage, 405/488/561 laser lines, and a 40×/1.3NA lens; or on an inverted Leica Thunder imaging system with individual LED lines, and 20×/0.8NA or 63×/1.4NA lenses. Confocal images were acquired at 8-bit. All thunder images were acquired at 16-bit, subjected to computational clearing, and then set to the same fluorescence range (e.g., 0–1000) within analysis cohorts before converting to 8-bit in Fiji. Representative super-resolution images in Figure 2g,h, and 3a were acquired with 4× Super Resolution by Optical Pixel Reassignment (SoRa) on an inverted spinning disk confocal microscope (Yokogawa CSU-W1 SoRa/Nikon Ti2-E Microscope) equipped with Hamamatsu Fusion BT cameras, and 20× water (0.95 NA. WD 1.0 mm) or 60× oil (1.49 NA. WD 0.14 mm) immersion lenses. All images within analysis cohorts were acquired using identical acquisition parameters or processed identically to maintain relative differences in fluorescence, and underwent native deconvolution and denoising using NIS-Elements Software.

4.5 | Quantification of ROI fluorescence and mitochondrial size and number

The mean fluorescence, average size and number of MCU- or COX4-labeled mitochondria were quantified using the image-analysis software Fiji (v. 2.1.0/1.53c, NIH) (Schindelin et al., 2012). When feasible, all analyses were done blind to genotype or condition. A representative 100 × 100 μm ROI was selected in SO, SR and SLM of each hippocampal section analyzed. For consistency, the brightest optical Z-slice that was in focus was chosen for each ROI. Cell bodies, blood vessels and tears in the tissue were avoided as much as possible when picking an ROI. A few of the ROIs were selected at an angle (by rotating the rectangular selection tool) to avoid the tissue edge or any of the above-mentioned features.

Fiji's *measure* tool was used to get the mean fluorescence ("mean gray value") of the cropped ROI images. Fluorescence was measured from the cropped 8-bit images with no other adjustments made. To get the average mitochondrial size and number, individual mitochondria were segmented using "Nucleus Counter" from Fiji's Cookbook Microscopy analysis plug-in. For the segmentation, we used an automated Otsu intensity threshold and a size threshold of 5–500 pixels with median 3 × 3 smoothing. The Otsu's thresholding algorithm searches for the threshold that minimizes the intraclass variance, defined as a weighted sum of variances of the two classes. Because images were individually thresholded, there was minimal influence of image intensity on the segmentation. A general "noise" threshold below which very few, if any, mitochondria were identified in the negative control images (without primary antibody) was used when necessary to adjust the automated Otsu threshold. Once the mitochondria were properly segmented, their areas were measured with the *measure* tool and exported in a .CSV file for further analysis and plotting in Python and Prism.

4.6 | Analysis of mitochondria in wild-type CA1 and CA2

40× confocal images of MCU-labeled mitochondria were segmented and quantified (as described above) from CA1 and CA2 of 3 wild-type mice, 4 hippocampal sections per mouse. 63× Thunder images of COX4-labeled mitochondria from CA1 and CA2 were similarly segmented and quantified in 7 different wild-type mice, ∼4 hippocampal sections per mouse. Because MCU and COX4 were imaged at different scales on different imaging systems, mitochondrial sizes cannot be directly compared between the MCU and COX4 populations.

Background fluorescence was measured by measuring the mean fluorescence of a similar ROI from negative control images (without primary antibody) of each layer in both CA1 and CA2. The background fluorescence was subtracted from the mean fluorescence of each ROI, and all the data was normalized to the cohort average (including SO, SR and SLM of both CA1 and CA2). For plotting, the sections were averaged together to get animal averages and SR and SLM of the same animal are paired with lines.

4.7 | Analysis of Mitotag mitochondria in CA2

Five male and female Mitotag mice were perfused, horizontally sectioned, and immunostained for GFP to boost the Mitotag signal (see Section 4.3). 16-bit images were acquired using 20×/0.8 NA and 63×/1.4 NA lenses on an inverted Leica Thunder imaging system with

identical acquisition parameters per section. Images were computationally cleared and scaled to the same fluorescence intensity per section. A 100 × 100 µm ROI was selected for CA2 SO, SR and SLM regions from 63× maximum intensity projected images, then cropped, and converted to 8-bit for analysis of mitochondrial area in Fiji. Individual mitochondria were segmented using the Cookbook Microscopy plugin "Nucleus Counter "and automatically threshold using the OTSU filter. The filter set "Watershed" was applied to represent the thresholding of the original ROI most accurately. All images were processed under 5 × 5 median smoothing settings, and a consistent particle size range (minimum: 10; maximum: 10,000). Mitochondria size was measured using the measuring tool as area and exported in a .CSV file for analysis. Mitochondrial area was normalized within individual mice and the average median area of mitochondria was reported across SO, SR, and SLM regions.

4.8 | Analysis of mitochondria after MCU overexpression in CA1

MCU-labeled mitochondria were quantified in SO, SR and SLM of CA1 in 6 AAV-MCU and 5 AAV-GFP control mice. A 100 × 100 µm ROI was chosen from 63× Thunder images from each dendritic layer. MCU fluorescence, mitochondrial size and mitochondrial number were measured for each ROI as described above. The AAV-MCU data was normalized to the average AAV-GFP control for each cohort ($n = 2$ cohorts). A two-way RM ANOVA was performed on the normalized data, pairing dendritic layers of the same animal together, to determine the overall effect of MCU overexpression and dendritic layer.

4.9 | Protein-retention expansion microscopy (ProExM)

40 µm horizontal mouse brain sections were expanded with 4× protein expansion microscopy (ProExM) as previously described in Campbell et al., 2021. All solutions were prepared as described by Asano et al., 2018. Sections to be expanded were incubated overnight in Acryloyl-X stock/PBS (1:100, ThermoFisher, A20770) at room temperature in the dark. Following incubation, the slices were washed twice with PBS for 15 min each at room temperature. The gelation solution was prepared by adding 384 µL of monomer solution, 8 µL 4-hydroxy-TEMPO inhibitor (1:200 [w/v], Sigma Aldrich, 176141), 8 µL TEMED accelerator (10% [v/v], Sigma Aldrich, T7024), and lastly 8 µL of APS initiator (10% [w/v], Sigma Aldrich, 248614) for each section. Sections were incubated in the gelation solution for 30 min at 4°C in the dark. Gelated sections were placed on gelation chambers constructed from microscope slides with coverslips as spacers. Our gelation chambers produce gels with the thickness of a single No. 1.5 coverslip (~0.15 mm thick). The chambers were filled with gelation solution and allowed to incubate at 37°C for 2 h in a humidified container. Following gelation, the gelation chamber was deconstructed and the gel was carefully removed from the chamber using a coverslip and Proteinase K-free digestion solution. Gels were then placed in digestion solution containing proteinase K (8 U/mL, New England BioLabs, P8107S) and digested for 4 h at room temperature.

For the AAV experiments, gels were placed in an alkaline buffer (100 mM Tris base, 5% [w/v] Triton X-100, 1% SDS) and digested with heat using an autoclave on the liquid cycle for 1 h at 121°C, which is a milder alternative to enzymatic digestion with Proteinase K, prior to antibody staining (Asano et al., 2018; Campbell et al., 2021). Proteinase K digested gels were immunostained prior to digestion instead. Gels were stained with DAPI (Sigma Aldrich, D9542; 1:10,000 in PBS) and MT-5 (gifted by Alex Kalyuzhny at Bio-Techne; 1:20,000 in PBS) for 30 min at room temperature with shaking. Kalyuzhny et al developed MT-5 as a novel mitochondrial marker specifically for use in fixed tissue (Kalyuzhny et al., 2021). MT-5 is a far-red fluorescence probe (655 nm excitation/669 nm emission) that localizes in mitochondria without cross-reacting with the cell nucleus or plasma membrane, and is highly photostable. Finally, the gels were washed twice with PBS for at least 20 min and either stored in PBS at 4C or fully expanded in npH20 for imaging. Images of CA2 SLM dendrites were acquired with 4× SoRa using a 20× water immersion lens (0.95 NA, WD 1.0 mm) and identical acquisition parameters on an inverted spinning disk confocal microscope (see Image acquisition and processing methods).

4.10 | Scanning electron microscope

This protocol was adapted from the protocol version 2 published by NCMIR at UCSD (Deerinck et al., 2022). Mice were anesthetized with sodium pentobarbital (euthanasia solution, 150 mg/kg) and perfused with ice-cold 0.1 M cacodylate buffer pH 7.4 containing 2.5% glutaraldehyde, 2% paraformaldehyde with 2 mM calcium chloride for 3 min. The brain was removed and fixed overnight at 4C in the same fixative before vibratome sectioning (Leica VT1000S) into 350-micron thick sections in the 0.1 M cacodylate buffer pH 7.4 with 2 mM calcium chloride. Sections were placed back in fixative for microdissection 3 days later. Hemisected brain sections were placed on wax paper with a drop of fixative and a 2 mm × 2 mm hippocampal microdissection was obtained per brain and placed back in fixative for further processing. Tissues were postfixed with 1.5% potassium ferrocyanide plus 2% osmium tetroxide then en bloc stained with incubations in thiocarbohydrazide solution, osmium tetroxide, uranyl acetate, and Walton's lead aspartate. Dehydration was performed by an ethanol gradient and finished in propylene oxide. Tissues were embedded in Epon 812. The embedded tissues were sectioned to 120 nm (Leica EM UC7 ultramicrotome), mounted on a silicon wafer, and imaged in a ThermoFisher Aprea Volumescope at 2 nm pixel size. Three 150 × 150 µm regions of interest were obtained per section (basal, proximal, distal CA2 dendrites). Images from one representative wild type mouse are shown. For the quantification, from each of three wild type mice, at least three 100 μm^2 ROIs were randomly selected per CA2 dendritic layer (basal, proximal, distal) from

the larger stitched SEM image. The experimenter was unable to be blinded to condition due to the obvious differences in dendritic and mitochondrial ultrastructure across layers. Cropped ROIs were processed with a 2 nm Gaussian blur. All mitochondria identified within an ROI were outlined using thresholding and the magic wand tool in Fiji. The resulting mitochondria ROIs were further manually refined using the selection brush tool. Mitochondrial diameter (feret's diameter) and area were measured and collated per layer across the three mice and the medians were compared using rank-based statistical tests.

4.11 | Statistical analyses

A custom Python code was written to parse the segmented data from Fiji, get the average size and number of mitochondria for each ROI, and combine the segmented data with the ROI fluorescence of each ROI. Statistical analyses were done in python (v3.7.9) or Prism (Graphpad Prism 9) with an alpha of 0.05 considered significant.

AUTHOR CONTRIBUTIONS

Conceptualization, Shannon Farris; methodology, Katy Pannoni, Daniela Gil, Mikel Cawley, Mayd Alsalman, Logan Campbell, Shannon Farris; formal analysis, Katy Pannoni, Daniela Gil, Mikel Cawley, Mayd Alsalman, Logan Campbell, Shannon Farris; investigation, Katy Pannoni, Daniela Gil, Mikel Cawley, Mayd Alsalman, Logan Campbell, Shannon Farris; writing—original draft, Katy Pannoni, Shannon Farris; writing—review and editing, Katy Pannoni, Mikel Cawley, Mayd Alsalman, Daniela Gil, Shannon Farris; visualization, Katy Pannoni, Mikel Cawley, Mayd Alsalman, Daniela Gil, Logan Campbell, Shannon Farris; supervision, Shannon Farris; funding acquisition, Shannon Farris.

ACKNOWLEDGMENTS

We thank the members of the Farris lab for providing feedback and critically reading this manuscript, as well as the Virginia Tech animal care staff and the Cell and Molecular Imaging Core for their support.

FUNDING INFORMATION

Research reported in this publication was supported by the National Institute of Mental Health of the NIH under award R00MH109626 and R01MH124997 to S.F. and by startup funds provided by Virginia Tech. The Serial Block Face Scanning Electron Microscope was acquired under NIH award 1S10OD026838-01A1. The funders had no role in the design of the study and collection, analysis, and interpretation of data and in writing the manuscript.

CONFLICT OF INTEREST STATEMENT

The authors declare that they have no competing interests.

DATA AVAILABILITY STATEMENT

Data available on request from the authors.

ORCID

Katy E. Pannoni https://orcid.org/0000-0002-4572-9757
Mikel L. Cawley https://orcid.org/0000-0002-0229-3471
Shannon Farris https://orcid.org/0000-0003-4473-1684

REFERENCES

Alexander, G. M., Brown, L. Y., Farris, S., Lustberg, D., Pantazis, C., Gloss, B., Plummer, N. W., Jensen, P., & Dudek, S. M. (2018). CA2 neuronal activity controls hippocampal low gamma and ripple oscillations. *eLife*, *7*(11), e38052. https://doi.org/10.7554/eLife.38052

Alexander, G. M., Martin, P., & Dudek, S. M. (2022). *Preferential expression of adeno-associated virus-packaged genetic cargo in hippocampal CA2 neurons. Program No. 743.14. 2022 neuroscience meeting planner*. Society for Neuroscience Online.

Asano, S. M., Gao, R., Wassie, A. T., Tillberg, P. W., Chen, F., & Boyden, E. S. (2018). Expansion microscopy: Protocols for imaging proteins and RNA in cells and tissues. *Current Protocols in Cell Biology*, *80*(1), e56. https://doi.org/10.1002/cpcb.56

Ashrafi, G., de Juan-Sanz, J., Farrell, R. J., & Ryan, T. A. (2020). Molecular tuning of the axonal mitochondrial Ca^{2+} uniporter ensures metabolic flexibility of neurotransmission. *Neuron*, *105*(4), 678–687.e5. https://doi.org/10.1016/j.neuron.2019.11.020

Baughman, J. M., Perocchi, F., Girgis, H. S., Plovanich, M., Belcher-Timme, C. A., Sancak, Y., Bao, R., Strittmatter, L., Goldberger, O., Bogorad, R. L., Koteliansky, V., & Mootha, V. K. (2011). Integrative genomics identifies MCU as an essential component of the mitochondrial calcium uniporter. *Nature*, *476*(7360), 341–345. https://doi.org/10.1038/nature10234

Bock, F. J., & Tait, S. W. G. (2020). Mitochondria as multifaceted regulators of cell death. *Nature Reviews Molecular Cell Biology*, *21*(2), 85–100. https://doi.org/10.1038/s41580-019-0173-8

Campbell, L. A., Pannoni, K. E., Savory, N. A., Lal, D., & Farris, S. (2021). Protein-retention expansion microscopy for visualizing subcellular organelles in fixed brain tissue. *Journal of Neuroscience Methods*, *361*(9), 109285. https://doi.org/10.1016/j.jneumeth.2021.109285

Chang, D. T. W., Honick, A. S., & Reynolds, I. J. (2006). Mitochondrial trafficking to synapses in cultured primary cortical neurons. *Journal of Neuroscience*, *26*(26), 7035–7045. https://doi.org/10.1523/Jneurosci.1012-06.2006

Chevaleyre, V., & Siegelbaum, S. A. (2010). Strong CA2 pyramidal neuron synapses define a powerful disynaptic cortico-hippocampal loop. *Neuron*, *66*(4), 560–572. https://doi.org/10.1016/j.neuron.2010.04.013

Dang, R., Zhou, Y., Zhang, Y., Liu, D., Miao, W., Liu, A., Jia, Z., & Xie, W. (2022). Regulation of social memory by lateral entorhinal cortical projection to dorsal hippocampal CA2. *Neuroscience Bulletin*, *38*(3), 318–322. https://doi.org/10.1007/s12264-021-00813-6

Deerinck, T. J., Bushong, E. A., Ellisman, M. H., & Thor, A. (2022). *Preparation of biological tissues for serial block face scanning electron microscopy (SBEM) V2*." Preprint. https://doi.org/10.17504/protocols.io.36wgq7je5vk5/v2

Devine, M. J., & Kittler, J. T. (2018). Mitochondria at the neuronal presynapse in health and disease. *Nature Reviews Neuroscience*, *19*(2), 63–80. https://doi.org/10.1038/nrn.2017.170

Divakaruni, S. S., Van Dyke, A. M., Chandra, R., LeGates, T. A., Contreras, M., Dharmasri, P. A., Higgs, H. N., Lobo, M. K., Thompson, S. M., & Blanpied, T. A. (2018). Long-term potentiation requires a rapid burst of dendritic mitochondrial fission during induction. *Neuron*, *100*(4), 860–875.e7. https://doi.org/10.1016/j.neuron.2018.09.025

Dudek, S. M., Alexander, G. M., & Farris, S. (2016). Rediscovering area CA2: Unique properties and functions. *Nature Reviews. Neuroscience*, *17*(2), 89–102. https://doi.org/10.1038/nrn.2015.22

Faitg, J., Lacefield, C., Davey, T., White, K., Laws, R., Kosmidis, S., Reeve, A. K., Kandel, E. R., Vincent, A. E., & Picard, M. (2021). 3D neuronal mitochondrial morphology in axons, dendrites, and somata of the aging mouse hippocampus. *Cell Reports*, *36*(6), 109509. https://doi.org/10.1016/j.celrep.2021.109509

Farris, S., Ward, J. M., Carstens, K. E., Samadi, M., Wang, Y., & Dudek, S. M. (2019). Hippocampal subregions express distinct dendritic transcriptomes that reveal differences in mitochondrial function in CA2. *Cell Reports*, *29*(2), 522–539.e6. https://doi.org/10.1016/j.celrep.2019.08.093

Fecher, C., Trovò, L., Müller, S. A., Snaidero, N., Wettmarshausen, J., Heink, S., Ortiz, O., Wagner, I., Kühn, R., Hartmann, J., Karl, R. M., Konnerth, A., Korn, T., Wurst, W., Merkler, D., Lichtenthaler, S. F., Perocchi, F., & Misgeld, T. (2019). Cell-type-specific profiling of brain mitochondria reveals functional and molecular diversity. *Nature Neuroscience*, *22*(10), 1731–1742. https://doi.org/10.1038/s41593-019-0479-z

Granatiero, V., Pacifici, M., Raffaello, A., De Stefani, D., & Rizzuto, R. (2019). Overexpression of mitochondrial calcium uniporter causes neuronal death. *Oxidative Medicine and Cellular Longevity*, *2019*, 1681254. https://doi.org/10.1155/2019/1681254

Groten, C. J., & MacVicar, B. A. (2022). Mitochondrial Ca^{2+} uptake by the MCU facilitates pyramidal neuron excitability and metabolism during action potential firing. *Communications Biology*, *5*(1), 900. https://doi.org/10.1038/s42003-022-03848-1

Han, X.-J., Yun-Fei, L., Li, S.-A., Kaitsuka, T., Sato, Y., Tomizawa, K., Nairn, A. C., Takei, K., Matsui, H., & Matsushita, M. (2008). CaM kinase Iα–induced phosphorylation of Drp1 regulates mitochondrial morphology. *Journal of Cell Biology*, *182*(3), 573–585. https://doi.org/10.1083/jcb.200802164

Helton, T. D., Zhao, M., Farris, S., & Dudek, S. M. (2019). Diversity of dendritic morphology and entorhinal cortex synaptic effectiveness in mouse CA2 pyramidal neurons. *Hippocampus*, *29*(2), 78–92. https://doi.org/10.1002/hipo.23012

Hitti, F. L., & Siegelbaum, S. A. (2014). The hippocampal CA2 region is essential for social memory. *Nature*, *508*(7494), 88–92. https://doi.org/10.1038/nature13028

Huntington, T. E., & Srinivasan, R. (2021). Astrocytic mitochondria in adult mouse brain slices show spontaneous calcium influx events with unique properties. *Cell Calcium*, *96*(6), 102383. https://doi.org/10.1016/j.ceca.2021.102383

Hutto, R. A., Bisbach, C. M., Abbas, F., Brock, D. C., Cleghorn, W. M., Parker, E. D., Bauer, B. H., Ge, W., Vinberg, F., Hurley, J. B., & Brockerhoff, S. E. (2020). Increasing Ca^{2+} in photoreceptor mitochondria alters metabolites, accelerates photoresponse recovery, and reveals adaptations to mitochondrial stress. *Cell Death & Differentiation*, *27*(3), 1067–1085. https://doi.org/10.1038/s41418-019-0398-2

Kalyuzhny, A. E., Taylor, J., Ptak, A., Wood, P., Miller, D., & Maple, H. (2021). *Novel mitochondria marker for staining formaldehyde fixed cells and tissue sections. Program No. P368.04. 2021 neuroscience meeting planner*. Society for Neuroscience Global Connectome Online.

Kamer, K. J., & Mootha, V. K. (2015). The molecular era of the mitochondrial calcium uniporter. *Nature Reviews. Molecular Cell Biology*, *16*(9), 545–553. https://doi.org/10.1038/nrm4039

Lee, A., Kondapalli, C., Virga, D. M., Lewis, T. L., Koo, S. Y., Ashok, A., Mairet-Coello, G., Herzig, S., Foretz, M., Viollet, B., Shaw, R., Sproul, A., & Polleux, F. (2022). Aβ42 oligomers trigger synaptic loss through CAMKK2-AMPK-dependent effectors coordinating mitochondrial fission and mitophagy. *Nature Communications*, *13*(1), 4444. https://doi.org/10.1038/s41467-022-32130-5

Lewis, T. L., Kwon, S.-K., Lee, A., Shaw, R., & Polleux, F. (2018). MFF-dependent mitochondrial fission regulates presynaptic release and axon branching by limiting axonal mitochondria size. *Nature Communications*, *9*(1), 5008. https://doi.org/10.1038/s41467-018-07416-2

Li, Z., Okamoto, K.-I., Hayashi, Y., & Sheng, M. (2004). The importance of dendritic mitochondria in the morphogenesis and plasticity of spines and synapses. *Cell*, *119*(6), 873–887. https://doi.org/10.1016/j.cell.2004.11.003

Llorente-Folch, I., Rueda, C. B., Pardo, B., Szabadkai, G., Duchen, M. R., & Satrustegui, J. (2015). The regulation of neuronal mitochondrial metabolism by calcium: Regulation of neuronal mitochondrial metabolism. *The Journal of Physiology*, *593*(16), 3447–3462. https://doi.org/10.1113/JP270254

Lopez-Rojas, J., de Solis, C. A., Leroy, F., Kandel, E. R., & Siegelbaum, S. A. (2022). A direct lateral entorhinal cortex to hippocampal CA2 circuit conveys social information required for social memory. *Neuron*, *110*(9), 1559–1572.e4. https://doi.org/10.1016/j.neuron.2022.01.028

Márkus, N. M., Hasel, P., Qiu, J., Bell, K. F. S., Heron, S., Kind, P. C., Owen Dando, T., Simpson, I., & Hardingham, G. E. (2016). Expression of MRNA encoding Mcu and other mitochondrial calcium regulatory genes depends on cell type, neuronal subtype, and Ca^{2+} signaling. *PLoS One*, *11*(2), e0148164. https://doi.org/10.1371/journal.pone.0148164

Pekkurnaz, G., & Wang, X. (2022). Mitochondrial heterogeneity and homeostasis through the lens of a neuron. *Nature Metabolism*, *4*(7), 802–812. https://doi.org/10.1038/s42255-022-00594-w

Popov, V., Medvedev, N. I., Davies, H. A., & Stewart, M. G. (2005). Mitochondria form a filamentous reticular network in hippocampal dendrites but are present as discrete bodies in axons: A three-dimensional ultrastructural study. *The Journal of Comparative Neurology*, *492*(1), 50–65. https://doi.org/10.1002/cne.20682

Qiu, J., Tan, Y.-W., Hagenston, A. M., Martel, M.-A., Kneisel, N., Skehel, P. A., Wyllie, D. J. A., Bading, H., & Hardingham, G. E. (2013). Mitochondrial calcium uniporter Mcu controls excitotoxicity and is transcriptionally repressed by neuroprotective nuclear calcium signals. *Nature Communications*, *4*(1), 2034. https://doi.org/10.1038/ncomms3034

Rangaraju, V., Lauterbach, M., & Schuman, E. M. (2019). Spatially stable mitochondrial compartments fuel local translation during plasticity. *Cell*, *176*(1–2), 73–84.e15. https://doi.org/10.1016/j.cell.2018.12.013

Rizzuto, R., De Stefani, D., Raffaello, A., & Mammucari, C. (2012). Mitochondria as sensors and regulators of calcium signalling. *Nature Reviews Molecular Cell Biology*, *13*(9), 566–578. https://doi.org/10.1038/nrm3412

Sajikumar, S., & Korte, M. (2011). Different compartments of apical CA1 dendrites have different plasticity thresholds for expressing synaptic tagging and capture. *Learning & Memory*, *18*(5), 327–331. https://doi.org/10.1101/lm.2095811

Schindelin, J., Arganda-Carreras, I., Frise, E., Kaynig, V., Longair, M., Pietzsch, T., Preibisch, S., Rueden, C., Saalfeld, S., Schmid, B., Tinevez, J. Y., White, D. J., Hartenstein, V., Eliceiri, K., Tomancak, P., & Cardona, A. (2012). Fiji: An open-source platform for biological-image analysis. *Nature Methods*, *9*(7), 676–682. https://doi.org/10.1038/nmeth.2019

Simons, S. B., Escobedo, Y., Yasuda, R., & Dudek, S. M. (2009). Regional differences in hippocampal calcium handling provide a cellular mechanism for limiting plasticity. *Proceedings of the National Academy of Sciences of the United States of America*, *106*(33), 14080–14084. https://doi.org/10.1073/pnas.0904775106

Spinelli, J. B., & Haigis, M. C. (2018). The multifaceted contributions of mitochondria to cellular metabolism. *Nature Cell Biology*, *20*(7), 745–754. https://doi.org/10.1038/s41556-018-0124-1

Sprenger, H.-G., & Langer, T. (2019). The good and the bad of mitochondrial breakups. *Trends in Cell Biology*, *29*(11), 888–900. https://doi.org/10.1016/j.tcb.2019.08.003

Srinivas, K. V., Buss, E. W., Sun, Q., Santoro, B., Takahashi, H., Nicholson, D. A., & Siegelbaum, S. A. (2017). The dendrites of CA2 and CA1 pyramidal neurons differentially regulate information flow in the Cortico-hippocampal circuit. *The Journal of Neuroscience: The Official*

Journal of the Society for Neuroscience, *37*(12), 3276–3293. https://doi.org/10.1523/JNEUROSCI.2219-16.2017

Stefani, D., Diego, A. R., Teardo, E., Szabò, I., & Rizzuto, R. (2011). A forty-kilodalton protein of the inner membrane is the mitochondrial calcium uniporter. *Nature*, *476*(7360), 336–340. https://doi.org/10.1038/nature10230

Stevenson, E. L., & Caldwell, H. K. (2014). Lesions to the CA2 region of the hippocampus impair social memory in mice. *European Journal of Neuroscience*, *40*(9), 3294–3301. https://doi.org/10.1111/ejn.12689

Steward, O. (1976). Topographic organization of the projections from the entorhinal area to the hippocampal formation of the rat. *The Journal of Comparative Neurology*, *167*(3), 285–314. https://doi.org/10.1002/cne.901670303

Stowers, R. S., Megeath, L. J., Górska-Andrzejak, J., Meinertzhagen, I. A., & Schwarz, T. L. (2002). Axonal transport of mitochondria to synapses depends on Milton, a novel drosophila protein. *Neuron*, *36*(6), 1063–1077. https://doi.org/10.1016/S0896-6273(02)01094-2

Sun, Q., Buss, E. W., Jiang, Y.-Q., Santoro, B., Brann, D. H., Nicholson, D. A., & Siegelbaum, S. A. (2021). Frequency-dependent synaptic dynamics differentially tune CA1 and CA2 pyramidal neuron responses to cortical input. *The Journal of Neuroscience*, *41*(39), 8103–8110. https://doi.org/10.1523/JNEUROSCI.0451-20.2021

Sun, Q., Srinivas, K. V., Sotayo, A., & Siegelbaum, S. A. (2014). Dendritic Na + spikes enable cortical input to drive action potential output from hippocampal CA2 pyramidal neurons. *eLife*, *3*(11), e04551. https://doi.org/10.7554/eLife.04551

Tang, Y.-g., & Zucker, R. S. (1997). Mitochondrial involvement in post-tetanic potentiation of synaptic transmission. *Neuron*, *18*(3), 483–491. https://doi.org/10.1016/S0896-6273(00)81248-9

Wang, X., & Schwarz, T. L. (2009). The mechanism of Ca^{2+}-dependent regulation of kinesin-mediated mitochondrial motility. *Cell*, *136*(1), 163–174. https://doi.org/10.1016/j.cell.2008.11.046

Wang, Y., Nguyen, N. X., She, J., Zeng, W., Yang, Y., Bai, X.-c., & Jiang, Y. (2019). Structural mechanism of EMRE-dependent gating of the human mitochondrial calcium uniporter. *Cell*, *177*(5), 1252–1261.e13. https://doi.org/10.1016/j.cell.2019.03.050

Wescott, A. P., Kao, J. P. Y., Lederer, W. J., & Boyman, L. (2019). Voltage-energized calcium-sensitive ATP production by mitochondria. *Nature Metabolism*, *1*(10), 975–984. https://doi.org/10.1038/s42255-019-0126-8

Zhao, M., Choi, Y.-S., Obrietan, K., & Dudek, S. M. (2007). Synaptic plasticity (and the lack thereof) in hippocampal CA2 neurons. *Journal of Neuroscience*, *27*(44), 12025–12032. https://doi.org/10.1523/JNEUROSCI.4094-07.2007

SUPPORTING INFORMATION

Additional supporting information can be found online in the Supporting Information section at the end of this article.

How to cite this article: Pannoni, K. E., Gil, D., Cawley, M. L., Alsalman, M. M., Campbell, L. A., & Farris, S. (2023). Layer-specific mitochondrial diversity across hippocampal CA2 dendrites. *Hippocampus*, *33*(3), 182–196. https://doi.org/10.1002/hipo.23512